Design and Analysis of a Programmable Receiver Front End with Time-Interleaved Baseband Analog-FIR Filtering

Sameed Hameed, *Member, IEEE*, and Sudhakar Pamarti, *Member, IEEE*

***Abstract*— This paper presents time-interleaving as an approach to improve the performance of programmable receiver front ends based on Filtering-by-Aliasing (FA). Using two parallel periodically time-varying paths, a sharp programmable filtering response is produced at RF, while achieving a good wideband S_{11}. The implemented receiver achieved a filter stop-band suppression of 70dB with only 4×BW transition bandwidth, while S_{11} is better than -10dB throughout most of the LO range. Analysis for achieved S_{11} and noise figure are shown, while detailing methods to improve filtering performance in presence of important circuit parasitics. The effect of mismatches between time-interleaved paths is also analyzed and quantified.**

***Index Terms*—Programmable receiver, mixer-first receiver, analog-FIR filter, sampled LPTV circuit, linear periodically time varying, high linearity, impedance matching, software-defined radio, passive mixer, time-interleaving**

I. Introduction

TRANSCEIVER designs have gradually evolved towards more programmability. The plethora of frequency bands that need to be supported in modern communication systems increasingly necessitate each transceiver to be built as a software-defined radio (SDR) [1]. In fact, radio concepts such as cognitive radios (CRs) [2] rely on such wide reconfigurability. While conventional radio front ends that use inductors and off-chip SAW/BAW filters have limited tunability, recent research has produced several approaches, such as discrete-time (DT) charge-domain signal processing [2-4], *N*-path filtering [4-9], and the related mixer-first receiver topology [10-15] to attain wide reconfigurability. Nevertheless, these approaches are generally limited in either linearity, impedance matching, or close-in blocker filtering. Hence, new approaches are necessary to solve this problem.

The concept of Filtering-by-Aliasing (FA) was recently proposed to achieve sharp anti-alias filtering [16]. The input to a sampler is multiplied with a periodic signal such that it is spread in the frequency domain. By choosing the periodic signal appropriately, it can be ensured that spread copies of out-of-band (OOB) signals cancel at the output of the sampler due to aliasing, leading to the moniker "Filtering-by-Aliasing". This concept was recently used in a receiver front end [17]. The receiver achieved sharp programmable filtering at RF, while maintaining linearity in the presence of close-in blockers by incorporating a mixer into a sampled integrate-and-dump circuit as shown in Fig. 1. By appropriately choosing the periodically time-varying resistor, $R(t)=R(t-T_s)$, an equivalent low-pass analog-FIR filter is realized from the input to the sampled output with the desired impulse response, $g(\tau)$, that can be upconverted to a desired center frequency by choosing the LO frequency of the additional mixer in series with $R(t)$.

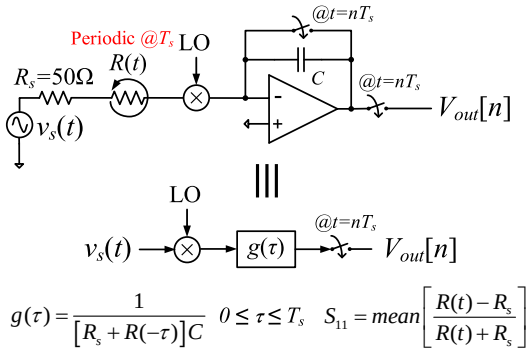

Fig. 1. The simple LPTV circuit used by the FA-based receiver in [17].

It was shown that by appropriately constraining the resistance variation, $R(t)$, a good wideband S_{11} is achievable [18]. Nevertheless, the filter stop-band suppression (A_{stop}) is limited due to the additional S_{11} requirements (in the example in Fig. 2(a), A_{stop} reduces from 60dB to 40dB with S_{11} constraints for T_s=0.1μs). The inherent sampling implies that the residual blockers alias in-band and cannot be further suppressed by additional filtering. For example, with the 3-tone input in Fig. 2(b), the 0dBm OOB blocker at 50MHz is only attenuated by 40dB before aliasing and falling on top of the in-band DC signal corrupting it. While A_{stop} can be potentially improved by increasing the length of $g(\tau)$, this requires increasing the output sampling period, T_s, in the circuit in Fig. 1 resulting in extra unfiltered aliasing bands. For example, doubling T_s to 0.2μs increases A_{stop} to 120dB (ignoring S_{11}

Manuscript received March 6, 2018; revised May 22, 2018; accepted July 31, 2018. This work was supported by the U.S. National Science Foundation under Award ECCS 1408647, the Broadcom Foundation under the Broadcom Fellowship Program, and the MediaTek Foundation under the MediaTek Fellowship Program.

S. Hameed and S. Pamarti are with the Electrical Engineering Department, University of California, Los Angeles, CA 90095, USA (e-mail: sameed@ucla.edu; spamarti@ucla.edu).

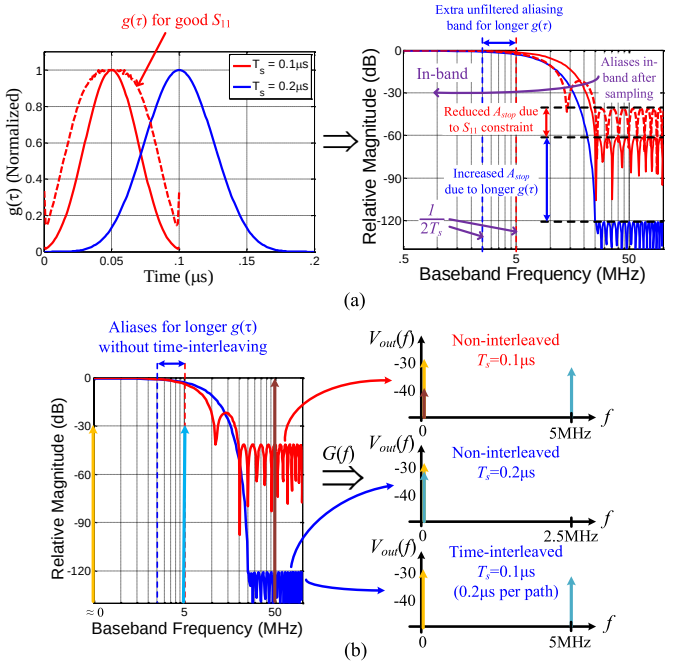

Fig. 2. (a) Limitations of the FA-based LPTV receiver in Fig. 1 due to S_{11} constraint and restricted filter length/output sampling rate. (b) Frequency spectrum of sampled output for different cases for an example 3-tone input.

constraints), but the 2.5 to 5MHz band aliases in-band as shown in Fig. 2(a). In the example in Fig. 2(b), this results in the 5MHz signal aliasing to DC, corrupting the in-band DC signal. Hence, an alternate method is needed to increase the filter length.

This paper details how time-interleaving can be applied to increase the filter length, while maintaining a sufficient output sampling rate. For example, in Fig. 2(b) the overall output sampling period can remain at 0.1μs (like in the original non-interleaved filter) by time-interleaving 2 paths each sampled with period 0.2 μs, and so the 5MHz signal no longer aliases to DC. As demonstrated in [19], time-interleaving allows for sharper filters with A_{stop} of up to 70dB without sacrificing linearity or noise figure (NF), while simultaneously achieving a good S_{11}. Section II develops time-interleaved FA and its realization in a receiver front end along with analysis for impedance matching and noise. Section III describes details of the circuit implementation and discusses important circuit non-idealities. Section IV discusses the measurement results from a fabricated prototype, followed by conclusions in Section V.

II. Time-Interleaved FA and Receiver Topology

Time-interleaving (or poly-phasing) is an increasingly popular technique used to increase the effective rate of operation of systems such as data converters, integration samplers, digital filters, etc. The concept is to simply time-multiplex multiple identical copies of a single system. Different copies are run by uniformly phase-shifted versions of a low-rate clock, but the time-multiplexed output effectively comes from a higher clock rate system. For example, consider the block diagram in Fig. 3, where each filter, $g(\tau)$, is like the filter from Fig. 1. Note that since the output of each filter is sampled with period $2T_s$, their lengths are $2T_s$ as well. However, if the sampling clocks (and corresponding variations and clocks in

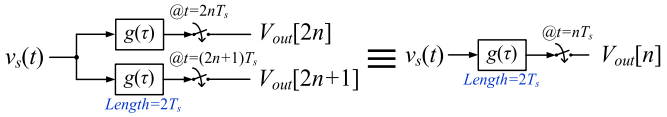

Fig. 3. Block diagram of a 2-way time-interleaved Filtering-by-Aliasing system.

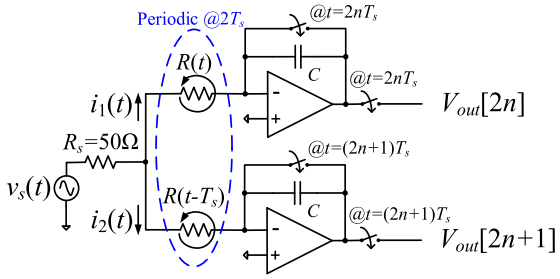

Fig. 4. Implementation of the baseband of the 2-way time-interleaved FA-based receiver based on two integrate-and-dump circuits.

each filter) are offset from each other by T_s, then the effective sampling period is T_s. Hence, the filter length is doubled while maintaining output sampling rate.

A. Circuit Implementation

An example time-interleaved FA system can be achieved using the circuit shown in Fig. 4. By utilizing two sampled integrate-and-dump circuits that are connected together at the source (antenna), each with sampling clocks and resistance variations that are time-shifted by T_s with respect to each other, the block diagram in Fig. 3 is realized. Note that the resistance variation, $R(t)$, is periodic with period $2T_s$ that is the sampling period in each path (the input impedance of the integrator is also included as part of $R(t)$). Then the output voltages can be calculated as:

$$V_{out}[2n] = \int_{t=2(n-1)T_s}^{2nT_s} \frac{i_1(t)}{C}\,dt$$
$$V_{out}[2n+1] = \int_{t=(2n-1)T_s}^{(2n+1)T_s} \frac{i_2(t)}{C}\,dt \qquad (1)$$

The currents can be simply calculated to be

$$i_1(t) = \frac{R(t-T_s)}{\left[R(t)+R(t-T_s)\right]}\frac{v_s(t)}{\left[R_s+R(t)\,\|\,R(t-T_s)\right]}$$
$$i_2(t) = \frac{R(t)}{\left[R(t)+R(t-T_s)\right]}\frac{v_s(t)}{\left[R_s+R(t)\,\|\,R(t-T_s)\right]} \qquad (2)$$

Using (1) and (2), and using the fact that $R(t)= R(t-2T_s)$, it can be verified that $V_{out}[n] = \int_{\tau=0}^{2T_s} g(\tau)v_s(nT_s-\tau)d\tau$, where

$$g(\tau) = \frac{R(T_s-\tau)}{\left[R(-\tau)+R(T_s-\tau)\right]}\frac{1}{\left[R_s+R(-\tau)\,\|\,R(T_s-\tau)\right]C} \quad 0\le\tau\le 2T_s, \qquad (3)$$

is the realized baseband FIR filter with length $2T_s$ (Note that longer filter lengths can be achieved by interleaving more paths. For example, for M-way time-interleaving M paths are present (with upfront resistances $R(t)$, $R(t-T_s)$, ..., $R(t-(M-1)T_s)$ where $R(t)=R(t-MT_s)$), each sampled with period MT_s in a time-interleaved fashion, thus realizing a filter $g(\tau)$ with length MT_s). The filter can then be designed as low-pass filters using digital FIR filter design techniques. This work uses linear optimization to generate such filters. Finally, N-phase passive mixers can be

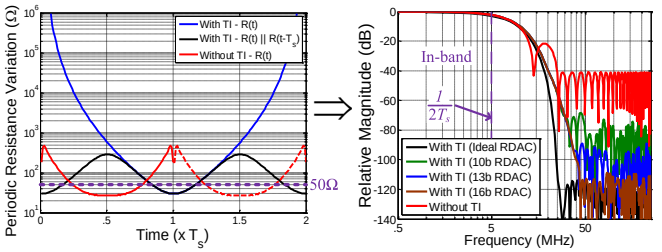

Fig. 5. Example resistance variation, and the corresponding magnitude of filter frequency responses for different accuracies of implementation of $R(t)$.

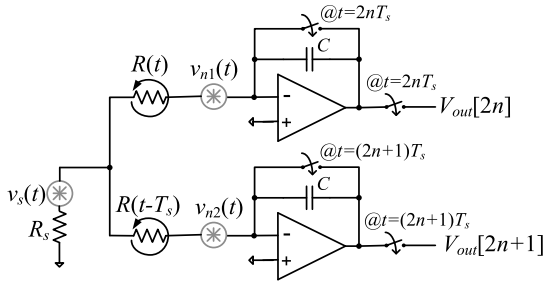

Fig. 6. Equivalent circuit for analysis of noise in the baseband of the receiver.

embedded into each time-interleaved path to achieve desired bandpass filters (this work utilizes 4-phase mixers like in [17]).

B. Impedance Matching

For the circuit in Fig. 4, the input impedance at any time instant is simply given by the parallel combination of time-varying resistances, $R(t)$ and $R(t\text{-}T_s)$ (which should include the op-amp input impedance and series impedances such as, for example, mixer switch resistance). Hence using the expression in Fig. 1, the S_{11} is given by

$$S_{11} = mean\left[\frac{R(t) \,||\, R(t-T_s) - R_s}{R(t) \,||\, R(t-T_s) + R_s}\right] \tag{4}$$

Note that the expression for S_{11} can be derived from basic relations between the incident and reflected voltages or using the concept of conversion matrices as shown in [18] and [20], respectively. Using (3), (4) can be simplified to give:

$$S_{11} = 1-\left(2R_sC\right) mean\left[g\left(\tau\right)+g\left(\tau+T_s\right)\right] \quad 0 \le \tau \le T_s. \tag{5}$$

The above expression is similar to the non-interleaved case [18], except for the additional term $g(\tau+T_s)$. In fact, for an M-way time-interleaved case the S_{11} can be similarly shown to be

$$S_{11} = 1-\left(2R_sC\right) mean\left[\sum_{m=0}^{M-1} g\left(\tau+mT_s\right)\right] \quad 0 \le \tau \le T_s.$$

In practice, this makes impedance matching far simpler with time-interleaving for any $g(\tau)$ [20]. For example, consider the filter to be a triangular window. For the non-interleaved case, such a filter required the minimum value attainable by $R(t)$, R_{min}, to be 0 to achieve S_{11}=0. However, R_{min} is usually set by other design constraints such as area/power [18]. In the 2-way time-interleaved case, the triangular window implemented as

$$g_{trng}(\tau) = \left[1-\frac{\left|T_s-\tau\right|}{T_s}\right]\frac{1}{2R_sC} \quad 0 \le \tau < 2T_s$$

only requires R_{min}= R_s while achieving S_{11}=0. This is far easier to implement given area/power constraints.

(5) can be further simplified by using the fact that FIR low-pass impulse responses peak at the center, and are small towards

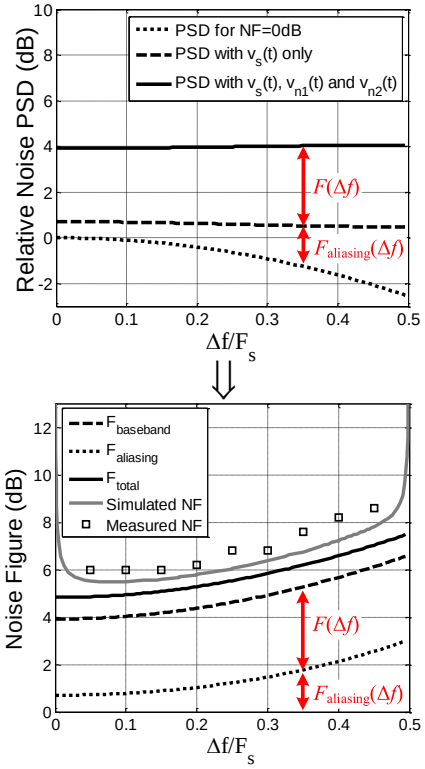

Fig. 7. Calculated baseband output noise PSDs and corresponding noise figure for the filter shown in Fig. 5.

the edges, i.e. for (3) $g(T_s) \gg g(0) \approx 0$. In that case, the minimum value attainable by $R(t)$, R_{min}, will be used at the peak of $g(\tau)$, i.e. $R(T_s)$= R_{min} and $R(0) \to \infty$, and so

$$g\left(0\right)+g\left(T_s\right) \approx g\left(T_s\right) = \frac{1}{\left(R_s+R_{min}\right)C} = g_{max},$$

where g_{max} is the peak value of the impulse response, $g(\tau)$. Hence, (5) can be expressed in terms of the normalized impulse response $g_{norm}^{max}(\tau) = g(\tau)/g_{max}$ as

$$S_{11} = 1-\frac{2R_s}{R_s+R_{min}} mean\left[g_{norm}^{max}(\tau)+g_{norm}^{max}(\tau+T_s)\right] \quad 0 \le \tau \le T_s. \tag{6}$$

Using (6), an additional constraint $|S_{11}| \le \beta$ can be added to the filter design problem, where β is the desired S_{11}. In practice, the S_{11} constraint has negligible effect on the filters obtained for reasonable values of R_{min}. Figure 5 shows a filter designed with a desired S_{11} of -20dB with and without time-interleaving for R_s=50Ω, and R_{min}=27Ω (similar to the implementation in this work). Up to 120dB of filter suppression can be achieved in this case, compared to only 40dB without time-interleaving. This is clear from the resistance variations, where the parallel combination easily manages to stay around 50Ω like the non-interleaved case, but the resistance variation, $R(t)$, itself can vary a lot more. Nevertheless, the actual suppression is limited by the accuracy of the resistance variation, $R(t)$. An accuracy of about 10 bits is necessary for attaining A_{stop}>70dB.

C. Noise Figure

The noise performance of the receiver can be analyzed based on the circuit shown in Fig. 6. The op-amps are considered to be simple g_m stages. Assuming the excess noise factor γ=1, the op-amp input-referred noise voltages and input impedances ($1/g_m$) can be lumped with the time-varying resistances [18].

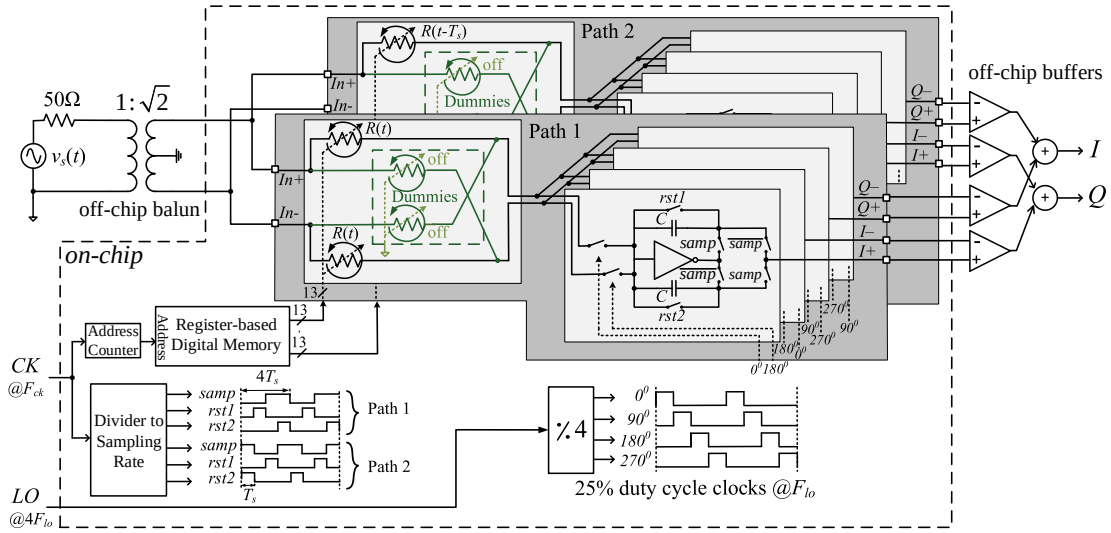

Fig. 8. Block diagram of the implemented receiver front end.

Hence, the noise sources considered are $v_s(t)$, $v_{n1}(t)$ and $v_{n2}(t)$ corresponding to the source, R_s, and time-varying resistances, $R(t)$ and $R(t\text{-}T_s)$, respectively. The noise sources are considered white and Gaussian with autocorrelations:

$$\begin{aligned} R_{ss}(t,\tau) &= E\left[v_s(t)v_s(t+\tau)\right] = 2kTR_s\delta(\tau), \\ R_{n_1n_1}(t,\tau) &= E\left[v_{n1}(t)v_{n1}(t+\tau)\right] = 2kTR(t)\delta(\tau), \\ R_{n_2n_2}(t,\tau) &= E\left[v_{n2}(t)v_{n2}(t+\tau)\right] = 2kTR(t-T_s)\delta(\tau). \end{aligned} \tag{7}$$

Using superposition, the output voltages can be obtained as:

$$\begin{aligned} V_{out}[2n] &= \int_{t=2(n-1)T_s}^{2nT_s} \frac{R(t-T_s)v_s(t)-\left[R_s+R(t-T_s)\right]v_{n1}(t)+R_sv_{n2}(t)}{C\left[R_sR(t)+R_sR(t-T_s)+R(t)R(t-T_s)\right]}dt, \\ V_{out}[2n+1] &= \int_{t=(2n-1)T_s}^{(2n+1)T_s} \frac{R(t)v_s(t)-\left[R_s+R(t)\right]v_{n2}(t)+R_sv_{n1}(t)}{C\left[R_sR(t)+R_sR(t-T_s)+R(t)R(t-T_s)\right]}dt. \end{aligned} \tag{8}$$

From (7) and (8), the autocorrelation of the output voltage samples can be calculated (similar to Appendix A in [18]) to be (9) as shown in the bottom of this page.

In (9), the first term in the numerator in each equation corresponds to noise from R_s, the second to noise from $R(t\text{-}T_s)$, and the last to the noise from $R(t)$. The autocorrelation, $R_{oo}[k]$ is non-zero only for sample delays $|k| \le 1$. This is intuitive since the noise contribution to output samples in each path are from independent values of the noise sources (the only memory in the system is due to the load capacitor that is reset after every sample). While the two paths do interact for adjacent samples (since both are operational at the same time), in practice the effect is small. For example, for the filter in Fig. 5, the ratio $|R_{oo}[1]/R_{oo}[0]| < 1\%$. This is because the paths interact only when $R(t) \approx R(t\text{-}T_s)$ that happens only for a short period of time.

To compute the noise figure, the noise power spectral density (PSD) can be calculated from the autocorrelation. The noise figure contribution due to aliasing (because of sampling), $F_{\text{aliasing}}(\Delta f)$, can be calculated by computing the noise PSD due to noise from R_s alone, $PSD_{R_s}(\Delta f)$ (computed from the autocorrelation with only the first term in the numerator in each equation in (9)), and comparing it with the PSD when the noise of R_s simply passes through the filter without aliasing, i.e.

$$F_{\text{aliasing}}(\Delta f) = \frac{PSD_{R_s}(\Delta f)}{2kTR_s\left|G(\Delta f)\right|^2} \quad |\Delta f| \le \frac{F_s}{2}, \tag{10}$$

where $G(f)$ is the frequency response of the filter, $g(\tau)$. Note that $PSD_{R_s}(\Delta f)$ can also be calculated from $G(f)$ directly as [18]

$$PSD_{R_s}(\Delta f) = 2kTR_s\sum_{n=-\infty}^{\infty}\left|G(\Delta f + nF_s)\right|^2.$$

Similarly, the noise figure contribution of the time-varying resistances can be computed by calculating the total PSD using all terms in (9), and comparing it with $PSD_{R_s}(\Delta f)$, i.e.

$$F(\Delta f) = \frac{PSD_{total}(\Delta f)}{PSD_{R_s}(\Delta f)} \quad |\Delta f| \le \frac{F_s}{2}. \tag{11}$$

Finally, when operated as a bandpass filter with a 4-phase 25% duty-cycle mixer, the noise figure degradation due to LO harmonics must be added as well as is given by [12]

$$F_{\text{harmonics}} = 1/\text{sinc}^2\left(1/4\right) \approx 0.91\text{dB}. \tag{12}$$

Thus, the total noise figure of the receiver is given by

$$\begin{aligned} F_{\text{total}}(\Delta f)\big|_{\text{dB}} &= 10\log_{10}\left[F(\Delta f)\times F_{\text{aliasing}}(\Delta f)\times F_{\text{harmonics}}\right] \\ &= F(\Delta f)\big|_{\text{dB}} + F_{\text{aliasing}}(\Delta f)\big|_{\text{dB}} + F_{\text{harmonics}}\big|_{\text{dB}}. \end{aligned} \tag{13}$$

$$R_{oo}[k] = E\left[V_{out}[n]V_{out}[n-k]\right] = \begin{cases} \dfrac{2kT}{C^2}\displaystyle\int_{t=0}^{2T_s}\frac{R_sR^2(t-T_s)+R(t-T_s)R_s^2+R(t)\left[R_s+R(t-T_s)\right]^2}{\left[R_sR(t)+R_sR(t-T_s)+R(t)R(t-T_s)\right]^2}dt & k=0 \\ \dfrac{2kT}{C^2}\displaystyle\int_{t=0}^{T_s}\frac{R_sR(t)R(t-T_s)-R(t-T_s)R_s\left[R_s+R(t)\right]-R(t)R_s\left[R_s+R(t-T_s)\right]}{\left[R_sR(t)+R_sR(t-T_s)+R(t)R(t-T_s)\right]^2}dt & k=\pm1 \\ 0 & \textit{else.} \end{cases} \tag{9}$$

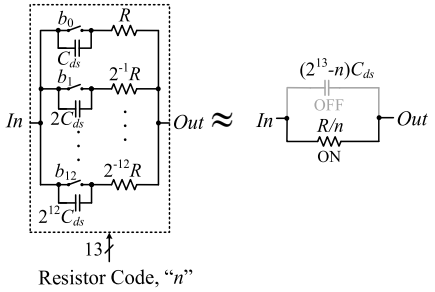

Fig. 9. Schematic of the 13-bit resistor DAC with annotated C_{ds} parasitic capacitance.

Figure 7 shows the calculated PSDs of the impedance-matched filter shown in Fig. 5. It can be seen that $F(\Delta f)|_{\text{dB}} \approx$ 3.4dB, and $F_{\text{aliasing}}(\Delta f=0)|_{\text{dB}}$ = 0.7dB. The total PSD is almost white, and $F(\Delta f)$ is almost constant across Δf. This confirms that the correlation between samples is small, and in fact $F(\Delta f)$ can be approximated by the non-interleaved case (where the PSDs are white) to give [18]

$$F(\Delta f) \approx 1 + \frac{mean\left[R(t)/\left(R_s + R(t)\right)^2\right]}{R_s\, mean\left[1/\left(R_s + R(t)\right)^2\right]}. \qquad (14)$$

This evaluates to 3.52dB that is an error of <0.2dB. It may be noted that S_{11} constraints will limit NF to be above 3dB [18] (similar to the main path of the noise-cancelling mixer-first receiver [12]). Noise cancellation methods can be employed to reduce the NF but are beyond the scope of this paper.

Figure 7 also shows the calculated NF along with simulated and measurement results for F_s=10MHz and F_{lo}=500MHz, with $F_{\text{baseband}}(\Delta f)=F(\Delta f)\times F_{\text{aliasing}}(\Delta f)$. The calculated average NF across frequencies is 5.8dB (the filter droop across the band is about 2.5dB). The results match well with calculations, with an additional ~0.5dB degradation observed in simulations due to input parasitic capacitance. The simulation results show a subtle phenomenon with flicker noise – since the two time-interleaved paths don't interact strongly, flicker noise from the baseband op-amp only appear in its corresponding path, i.e., each op-amp's flicker noise appear at the final output only during either odd or even-numbered samples. Thus, half of flicker noise power is shifted up to half of the net output sampling frequency (F_s/2=5MHz), thus reducing flicker noise corner frequency by half compared to the non-interleaved case [18]. In Fig. 7, the corner frequency is ~30kHz.

III. Implementation and Non-idealities

The block diagram of the implemented RF front end is shown in Fig. 8. The 50Ω input is converted to a differential 100Ω input using an external 1:$\sqrt{2}$ balun transformer. The receiver IC consists of two identical time-interleaved paths. In each path the differential balun output is connected to a pair of LPTV resistors, $R(t)$, that are built as nominally 13b binary-scaled resistor DACs (RDACs). The RDAC control bits are periodic with the period, $2T_s$, and are generated from an on-chip register-based memory that is read out cyclically based on the input clock, F_{ck}. In each path, a set of dummy RDACs (identical to the main RDACs, but with all switches turned OFF) are connected across the main RDACs in a cross-coupled fashion. This arrangement can be shown to improve the dynamic range

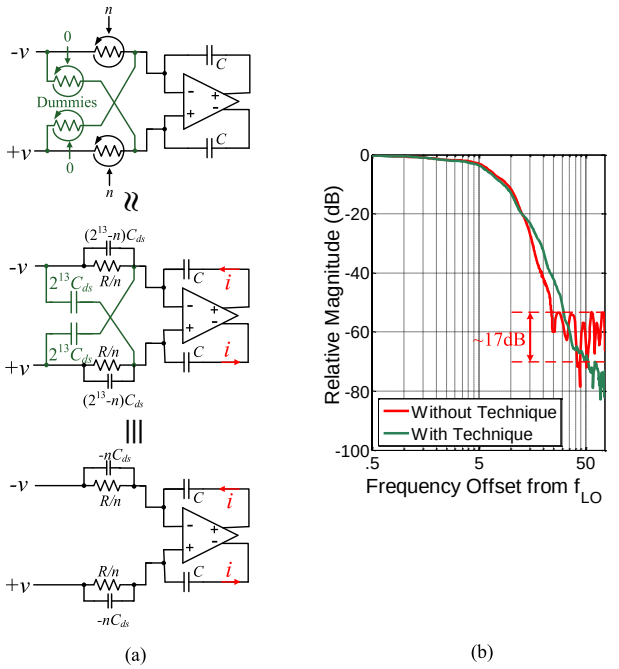

Fig. 10. (a) Alleviation of parasitic C_{ds} capacitance using cross-coupled dummy RDACs. (b) Measured improvement in the filter magnitude response due to addition of cross-coupled dummy RDACs.

of the RDACs.

In each path, the differential RF current is mixed down to baseband by a set of 25% duty-cycle mixer switches switching at the LO frequency, F_{lo}, that realizes a 4-phase mixer. The mixer switches use transmission gates with equal-sized PMOS and NMOS devices (to minimize LO feed-through and charge injection) and have a resistance of about 3Ω. The baseband integrate-and-dump blocks utilize self-biased inverter-based op-amps, with sampling and reset clocks generated by dividing the input clock, F_{ck}. Each capacitor bank, C, is built as a ping-pong structure, allowing one capacitor to be connected across the op-amp, while the voltage stored on the other can read and reset using the clocks shown. The capacitor banks use MIM capacitors and are tunable from 10-70pF to allow for a wide range of filter bandwidths, and their parasitics have no noticeable effect on performance. The op-amps themselves are self-biased due to the ping-pong action. Each op-amp consists of high-V_t PMOS and NMOS devices of length 180nm to increase gain to about 35dB and to reduce the flicker noise corner, and has a transconductance, g_m, of 125mS. The g_m is chosen to minimize noise figure contribution, as well as to minimize the op-amp input impedance ($1/g_m$), thus reducing the minimum resistance achievable at the front end, R_{min}, to aid in impedance-matching (op-amp gain, and g_m do not significantly affect A_{stop} [18]). To achieve the time-interleaving operation the RDAC controls and the sampling and reset clocks for the two paths are offset in time by T_s. Each path can be turned ON or OFF independently to test for non-interleaved operation. The LO switches connected to the negative input can also be turned OFF for single-ended operation.

The most important non-idealities are now considered and their effects shown.

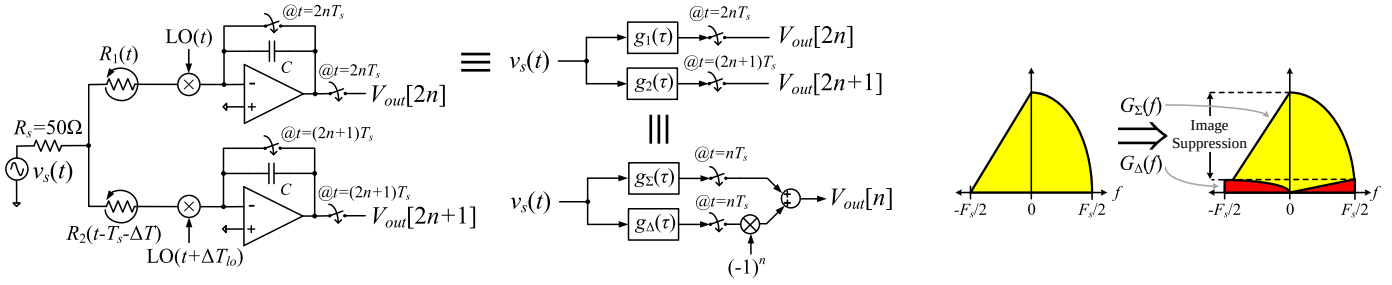

Fig. 11. (a) Model to analyze the effect of circuit mismatches on the filter. (b) Example of effect of mismatches on an in-band signal.

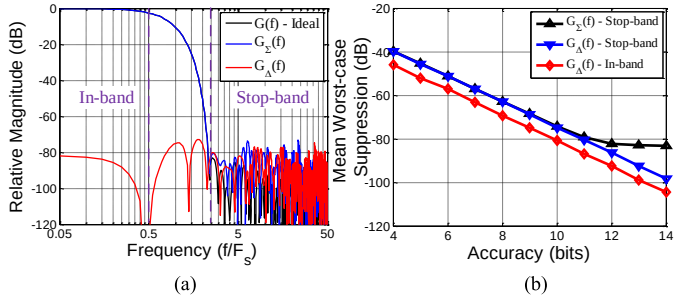

Fig. 12. (a) Desired and image filter responses with 13b RDACs calibrated to 10b accuracy. (b) Effect of random resistance mismatch on filter suppression due to limited calibration accuracy of 13b RDACs.

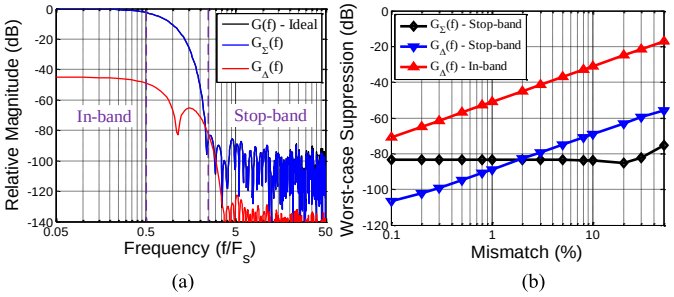

Fig. 13. (a) Desired and image filter responses with mismatch α_R=2% between RDACs. (b) Effect of systematic resistance mismatch between RDACs on filter performance.

A. *RDAC Parasitics*

The heart of the receiver front end are the 13-bit RDACs shown in Fig. 9. As shown, the RDAC is implemented in a binary-scaled fashion, with each branch consisting of an *rppoly* resistor, R, in series with a transmission gate control switch (with equal-sized PMOS and NMOS devices) with resistance, R_{sw}. The minimum RDAC resistance was designed to be about 15.7Ω. R_{sw}:R was set to 1:4 as a trade-off between linearity, switch parasitics, and power consumption.

As discussed in [18], the primary contributor to lower A_{stop} is the C_{ds} capacitance that is present mainly present due to routing. As shown in Fig. 9, when the RDAC is set to a resistor code of n, the ON-paths contribute to give the desired resistance of R/n. However, the OFF-path C_{ds} capacitance add in parallel to give a capacitance of $(2^{13}\text{-}n)C_{ds}$, thus leading to a corner frequency of

$$\omega_{corner} = \frac{n}{2^{13}-n}\frac{1}{RC_{ds}} \tag{15}$$

Note that ω_{corner} reduces for smaller n, and so the RDAC does not realize large resistance values. Hence the RDAC dynamic range is degraded, leading to lower A_{stop} (a dynamic range of ~10b is needed for A_{stop}>70dB as shown in Fig. 5).

To alleviate this problem, consider the differential circuit in Fig. 10(a). The main RDACs are set to a code, n, while the additional dummy RDACs (connected in a cross-coupled fashion) are OFF, i.e. set to a code of 0. From the equivalent circuit, it can be seen that the differential output current is given by

$$i = \frac{n}{R}v - nC_{ds}\frac{dv}{dt} \tag{16}$$

This is because parasitic currents drawn by a capacitance of $2^{13}C_{ds}$ in the main RDACs simply circulate through the cross-coupled dummy RDACs. Thus, $2^{13}C_{ds}$ of parasitic capacitance in the main RDACs are neutralized, implying that the equivalent circuit can be drawn as the final circuit in Fig. 10(a). Thus, the corner frequency of the RDACs now become

$$\omega_{corner} = \frac{1}{RC_{ds}} \tag{17}$$

that is constant with respect to code, n. Moreover, this corner frequency is typically much higher than the frequency range of interest and so RDAC dynamic range is restored. Measurement results for an example filter shown in Fig. 10(b) confirm the utility of this technique, with A_{stop} improved by 17dB. Note that this technique will work with a single-ended input as well, i.e., without the negative input and the RDACs connected to it. The output differential current in the single-ended case can also be verified to be given by (16).

B. *Path Mismatches*

Figure 11(a) shows important sources of mismatch in the time-interleaved implementation. The time-varying resistance values, $R_1(t)$ and $R_2(t)$ are nominally equal to their ideal value $R(t)$ (as are capacitors C_1 and C_2 to C), but can be unequal due to random or systematic mismatch between RDACs leading to gain mismatch between paths. Further, the timing offset between the resistance variations can be slightly skewed to $T_s+\Delta T$ with ΔT (ideally 0) being the timing skew. Similarly, the LO signals may be skewed by ΔT_{lo} between paths as well. This results in slightly mismatched baseband impulse responses in the two paths (instead of $g(\tau)$ from (3)) given by

$$g_1(\tau) = \frac{R_2(T_s-\tau+\Delta T)}{\left[R_1(-\tau)+R_2(T_s-\tau+\Delta T)\right]}\frac{1}{\left[R_s+R_1(-\tau)\,\|\,R_2(T_s-\tau+\Delta T)\right]C_1}$$

$$g_2(\tau) = \frac{R_1(T_s-\tau)}{\left[R_1(T_s-\tau)+R_2(-\tau+\Delta T)\right]}\frac{e^{j\phi}}{\left[R_s+R_1(T_s-\tau)\,\|\,R_2(-\tau+\Delta T)\right]C_2} \quad 0\le\tau\le 2T_s, \tag{18}$$

where ϕ is the phase offset introduced due to LO mismatch. These can be further expressed as shown in Fig. 11(a) with

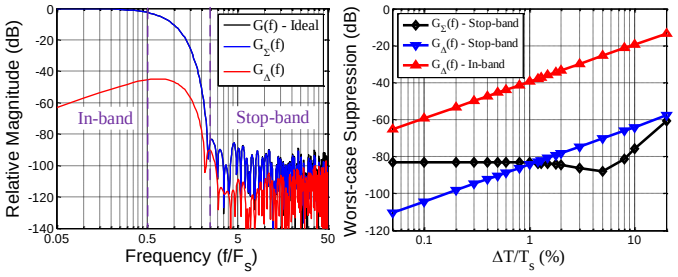

(a) (b)

Fig. 14. (a) Desired and image filter responses with timing skew of 0.5% of sampling period between RDAC controls of the two paths. (b) Effect of timing skew between RDAC controls of the two paths on filter performance.

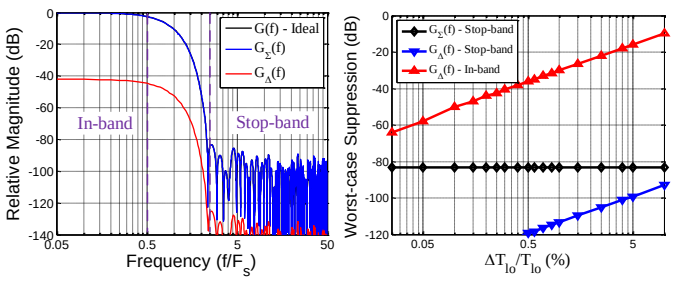

(a) (b)

Fig. 15. (a) Desired and image baseband filter responses with timing skew of 0.25% of LO period between LO signals of the two paths. (b) Effect of timing skew between LO signals of the two paths on filter performance.

$$g_\Sigma(\tau)=\frac{g_1(\tau)+g_2(\tau)}{2},\ g_\Delta(\tau)=\frac{g_1(\tau)-g_2(\tau)}{2}, \qquad (19)$$

where $g_\Sigma(\tau)$ is the desired filter impulse response (ideally equals $g(\tau)$ from (3)), and $g_\Delta(\tau)$ is the undesired image filter response that results due to the imperfect cancellation of aliasing images (like in case of mismatch in a time-interleaved ADC). While the desired filter, $g_\Sigma(\tau)$, filters the input and aliases to the ideal sub-sampled discrete-time frequency, ω_{des}, the undesired image filter, $g_\Delta(\tau)$, aliases the filtered signal to the image frequency of ($\omega_{des}\pm\pi$). Figure 11(b) shows the effect of these filters on an example in-band signal. The difference in gain between the desired and image filters gives the image suppression of the system. Since the image for an in-band signal is the signal itself, the in-band image suppression required is typically determined by the overall signal-to-noise ratio (SNR) requirement of the system (typically 30dB or more is sufficient). In the stop-band, both the desired and image filters should attain the desired A_{stop}. Thus, the effects of various mismatches can be quantified through the frequency responses of the filters, $g_\Sigma(\tau)$ and $g_\Delta(\tau)$.

1) RDAC Resistance Mismatch

The binary-scaled RDACs are built as parallel combination of unit cells that can be expected to be randomly mismatched. Hence the RDACs have to be calibrated to achieve the accuracy required for A_{stop} of 70dB. To model the effect of calibration, random RDAC code vs. resistance curves are generated such that for a code of n, the resistance produced by the RDAC is modeled to be R/k, where k is uniformly distributed in [n - Δ/2, n + Δ/2], with Δ set by the calibration accuracy (ideally a truncated Gaussian, uniform distribution is a worst-case approximation). For example, in an M-bit RDAC calibrated to B bits of accuracy, $\Delta=2^{M-B}$. Using such a model and the ideal resistance codes, the filters from (18) and thereafter (19) can be calculated for generating their frequency responses.

As an example, Fig. 12(a) shows the frequency responses for a randomly generated case of 13-bit RDACs calibrated to 10-bit accuracy. Comparing the filter, $G(f)$ obtained for ideal 13-bit RDACs to the desired $G_\Sigma(f)$, it is seen that A_{stop} worsens due to mismatch. The stop-band achieved is similar to that of the image filter, $G_\Delta(f)$. Figure 12(b) plots the variation of mean worst-case suppression in the stop-band for $G_\Sigma(f)$ and $G_\Delta(f)$, and mean worst-case suppression in-band for $G_\Delta(f)$ averaged over 1000 randomly generated RDAC profiles (for each accuracy level) for 13-bit RDACs. A_{stop} worsens by ~6dB when precision reduces by 1 bit (expected due to additional quantization noise introduced in the filter impulse responses). To achieve A_{stop} better than 70dB, more than 9 bits of accuracy is necessary. This is identical to the RDAC accuracy requirement noted in Fig. 5.

A second concern in terms of RDAC resistance values is systematic mismatch between RDACs in the two time-interleaved paths. For example, consider a systematic mismatch of α_R between $R_1(t)$ and $R_2(t)$ in Fig. 11, i.e. $R_2(t)/R_1(t)=(1-\alpha_R/2)/(1+\alpha_R/2)$. The effect of such an offset on the filters can be easily calculated using (18) and (19). For example, Fig. 13(a) shows the case for α_R=2%. It is seen that while stop-band suppression is unaffected, the suppression of the image filter, $G_\Delta(f)$, in-band is much lower than for random variation. Nevertheless, the required in-band suppression is much lower in general, since the aliasing band is the wanted signal band itself (as described previously). Figure 13(b) plots the variation of worst-case suppression for the desired and undesired filters as a function of α_R calculated using (18). To maintain in-band image suppression above 40dB, α_R should be below 3%. RDAC calibration should alleviate systematic mismatch as well.

The effect of mismatch between RDACs is hard to calculate without resorting to explicit calculations using (18) as the gain mismatch is periodically time-varying. On the other hand, the effect of capacitor mismatch is far easier to calculate. A mismatch of α_C between C_1 and C_2, i.e. $C_2/C_1=(1-\alpha_C/2)/(1+\alpha_C/2)$ gives

$$\frac{g_2(\tau)}{g_1(\tau)}=\frac{1+\alpha_C/2}{1-\alpha_C/2}\Rightarrow\frac{g_\Delta(\tau)}{g_\Sigma(\tau)}=-\frac{\alpha_C}{2}. \qquad (20)$$

Thus, to maintain in-band image suppression above 40dB, α_C should be below 2%. Further, such a constant gain mismatch can be easily corrected at the output samples of each path.

2) Timing Skew between RDACs

Timing skew between RDAC controls of the two time-interleaved paths can have a severe impact on the image filter. For example, Fig. 14(a) shows the effect of a timing skew of ΔT that is 0.5% the net sampling period, T_s, explicitly calculated with (18). Like the case of systematic RDAC mismatch, the stop-band suppression is unaffected but the in-band suppression of the image filter, $G_\Delta(f)$, is only about 45dB (sufficient for typical SNR requirements). Figure 14(b) plots the variation of worst-case suppression for the desired and undesired filters as a function of percentage timing skew. It can be seen that to maintain in-band image suppression above 40dB, skew of less than 1% is necessary.

The effect of the skew can be approximated by assuming that for small ΔT, the interactions between paths are unaffected (i.e. $R_2(\tau+\Delta T)\approx R_2(\tau)$ in $g_1(\tau)$ and $R_1(\tau)\approx R_1(\tau+\Delta T)$ in $g_2(\tau)$ to imply

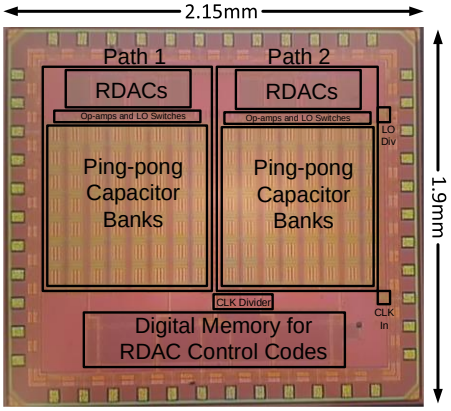

Fig. 16. Chip micrograph.

that for a given path under consideration, the resistance variation in the other path is similarly skewed in time so that interaction with it is unchanged). This simply means that the impulse responses themselves are delayed, giving

$$g_1(\tau)\approx g(\tau),\ g_2(\tau)\approx g(\tau-\Delta T)\approx g(\tau)-\Delta T\frac{d}{d\tau}g(\tau)$$

$$\Rightarrow g_\Sigma(\tau)\approx g(\tau),\ g_\Delta(\tau)\approx\frac{\Delta T}{2}\frac{d}{d\tau}g(\tau)\xrightarrow{\mathcal{F}}\frac{G_\Delta(f)}{G_\Sigma(f)}\approx j\pi f\Delta T.$$

This explains the in-band first-order high-pass shape of the image filter seen in Fig. 14(a). To calculate the peak amplitude of $G_\Delta(f)$ it may be noted that $G_\Sigma(f)$ is designed to be flat up to $F_s/2$ (where it has relative gain of ≈ -3dB) before falling sharply. Thus $G_\Delta(f)$ peaks at $\approx F_s/2$ with a peak relative gain of

$$\left|G_\Delta(f)\right|_{\max}\approx\left[20\log_{10}\left(\pi F_s\Delta T/2\right)-3\right]\text{dB}. \qquad (21)$$

This result matches Fig. 14(b), with the calculated image suppression being 39dB for $\Delta T=T_s/100$. While considering the issue of timing skew, it must be noted that the RDAC controls are switched at a clock frequency, F_{ck}. Hence, the RDAC controls can be easily shifted in steps of $T_{ck}=1/F_{ck}$ to achieve a maximum skew of $T_{ck}/2$. Thus, if $T_{ck}/T_s\leq 2\%$, i.e. an oversampling factor (T_s/T_{ck}) of 50 or more, image suppression is ensured to be better than 39dB. Generally, F_{ck} is decided based on the suppression desired for the passband image generated at a frequency offset of F_{ck} in the filter frequency response due to sampled-and-held implementation of resistance variations [18]. Therefore, timing skew introduces an additional constraint on the choice of F_{ck}.

3) *LO Mismatch between Paths*

Finally, timing skew between LO signals of the two paths may also contribute to unwanted images in the output. Figure 15(a) shows the effect of a timing skew of ΔT_{lo} that is 0.25% of the LO period. The LO signals are assumed to be ideal 25% duty-cycle square-wave signals, and the filters shown are the baseband equivalent filters of the bandpass filters obtained at the LO fundamental frequency. In this case, the desired filter, $G_\Sigma(f)$, seems unaffected, and the magnitude of the image filter, $G_\Delta(f)$, appears to be the same as $G_\Sigma(f)$, but shifted down by about 40dB. Figure 15(b) plots the variation of worst-case suppression for the desired and undesired filters as a function of percentage timing skew. It can be seen that to maintain in-band image suppression above 40dB, skew of less than 0.3% is necessary. The effect of LO skew can also be easily calculated by noting that it only introduces a phase rotation in the

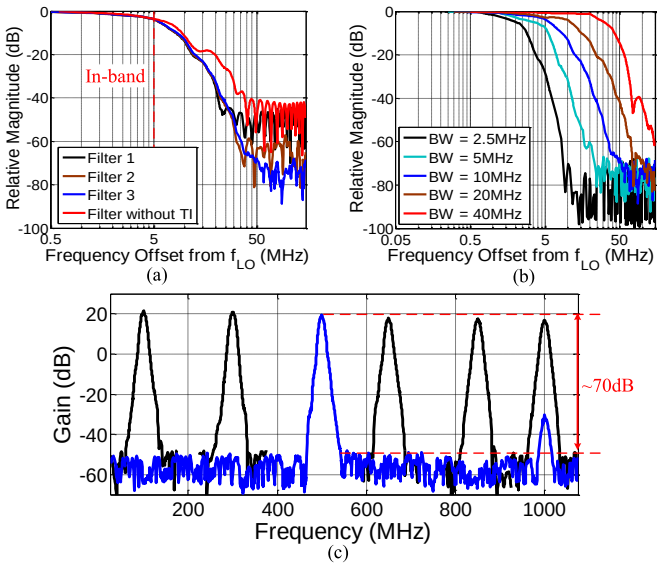

Fig. 17. (a) Measured 10MHz RF BW (5MHz baseband BW) filter responses. (b) Filter 3 responses for BW tuned from 2.5-40MHz. (c) Filter 3 responses for the LO frequency varied from 0.1-1GHz.

corresponding baseband equivalent filter. Hence, for the LO frequency of F_{lo}, the phase shift at the fundamental due to skew is given by $\phi=2\pi F_{lo}\Delta T_{lo}$. Thus, the baseband filters are given by

$$\begin{aligned}g_1(\tau)&=g(\tau)\\ g_2(\tau)&=e^{j\phi}g(\tau)\end{aligned}\Rightarrow\begin{aligned}2g_\Sigma(\tau)&=(1+e^{j\phi})g(\tau)\\ 2g_\Delta(\tau)&=(1-e^{j\phi})g(\tau).\end{aligned}$$

This shows why the magnitudes of $G_\Sigma(f)$ and $G_\Delta(f)$ are identical, except for a gain shift. For small ϕ,

$$\frac{g_\Delta(\tau)}{g_\Sigma(\tau)}\approx -j\frac{\phi}{2}. \qquad (22)$$

Hence, for 40dB image suppression, ϕ has to be about 1.15° or 0.32%. Nevertheless, a known constant LO skew can be easily corrected for by phase rotating the output samples of the corresponding path.

IV. Measurement Results

The receiver front end IC was fabricated in TSMC 1P6M 65nm CMOS process and was packaged in a 40-pin 5mm×5mm QFN package. Figure 16 shows the micrograph of the implemented IC. It has an active area of 2.3mm^2, of which 70% is occupied by capacitors. The capacitor area can be significantly reduced when designed for operation with only higher filter bandwidths.

A supply voltage of 1.2V is used for the op-amps, the LO dividers, as well as the drivers for controlling the resistor DAC and LO switches. The DC bias of the entire chain is set to around 0.6V due to the op-amp biasing at reset. The rest of the circuitry runs on a 1V supply. For a 10MHz bandwidth (BW) filter centered on F_{lo}=500MHz, a current of 64.7mA is drawn from the 1.2V supply, with each op-amp consuming 6.5mA, the LO divider and switch drivers consuming about 12.7mA, while the other digital blocks draw 7.75mA from the 1V supply for a nominal clock frequency of F_{ck}=1GHz. The system was verified to work up to F_{ck} =2GHz for use with higher filter bandwidths.

The sampled-and-held outputs of the time-interleaved paths are buffered and combined externally for measurements. Figure 17(a) shows the measured filter responses in three different

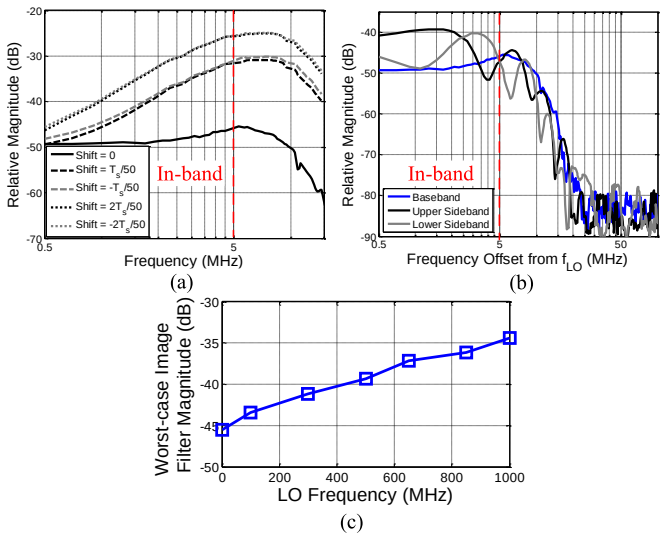

Fig. 18. (a) Measured baseband image filter responses (5MHz baseband BW) in filter 3 configuration with intentional timing shifts in RDAC controls of one path. (b) Baseband image filter compared to image filter (both upper and lower sidebands) for F_{lo}=500MHz (10MHz RF BW in filter 3 configuration). (c) Variation of worst-case image filter magnitude with LO frequency, F_{lo}.

time-interleaved 10MHz BW filter configurations (filters 1-3) that vary in transition BW and attenuation. The transition BWs for filters 1, 2, and 3 were 17MHz, 25MHz, and 40MHz respectively, while the achieved stop-band rejection was observed to be better than 45dB, 58dB, and 70dB respectively. In comparison, the measured non-interleaved filter achieved a stop-band rejection of only 40dB with a transition BW of 35MHz. The filter BW was varied from 2.5-40MHz by varying T_s, and the results are shown in Fig. 17(b). The receiver gain obtained for the 10MHz BW filter with C=70pF was 23dB. The gain scales linearly with T_s and inversely with C. F_{lo} was also varied from 100MHz to 1GHz as shown in Fig. 17(c). The gain reduced by ~4dB from F_{lo} =100MHz to 1GHz.

Figure 18 shows measured image filter responses (normalized to peak of corresponding desired filter responses) with the most stringent filter 3 configuration, all with 5MHz baseband BW (T_s=100ns). Figure 18(a) shows that the baseband filter by itself has at least ~46dB image rejection that improves to ~50dB at DC. Shifting the RDAC control codes of one path by T_s/50 and its multiples worsens image rejection (as is expected due to the intentionally introduced timing skew). Image rejection degrades to ~31dB and ~25dB for shifts of T_s/50 and T_s/25, respectively, matching calculations in Fig. 14(b) and from (21). Figure 18(b) shows the image filter for an RF filter with F_{lo}=500MHz. Image rejection degrades to ~39dB due to LO phase mismatches. Note that the image filter upper and lower sidebands are not identical due to the interaction between effects of timing skews in LO and RDAC controls. Finally, Fig. 18(c) shows the variation of worst-case image rejection with F_{lo}. The rejection degrades with higher F_{lo} that is expected for a fixed timing skew between paths. The worst-case of 34dB for F_{lo}=1GHz is close to the 6dB degradation expected as per (22) with respect to F_{lo}=500MHz case.

Figure 19 shows linearity measurements for a 10MHz BW filter 1 configuration with F_{lo}=500MHz and C=70pF. While the in-band IIP_3 was measured to be about +8.2dBm, OOB IIP_3 was

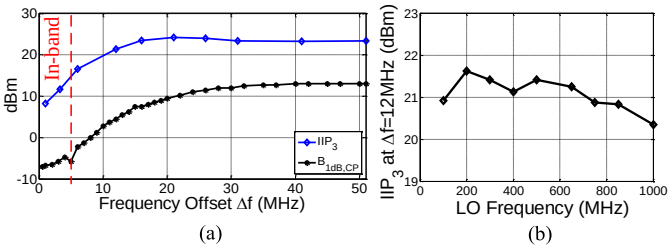

Fig. 19. (a) Measured IIP_3 and $B_{1dB,CP}$ for different frequency offsets from LO. (b) OOB IIP_3 at Δf=12MHz for LO varied from 0.1-1GHz, both for a 10MHz RF BW filter in filter 1 configuration.

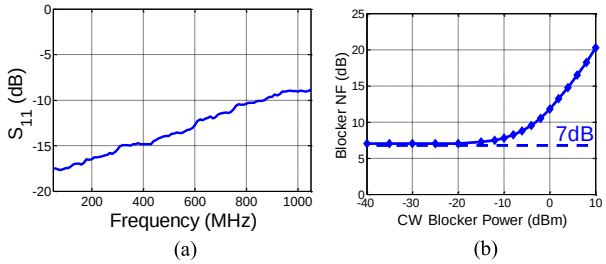

Fig. 20. (a) Measured S_{11} for filter 1 configuration. (b) Measured noise figure in the presence of a continuous wave blocker at Δf=30MHz for a 10MHz RF BW filter with F_{lo}=500MHz in filter 1 configuration.

better than +21.4dBm, and OOB IIP_2 was better than +64dBm without calibration, both at 12MHz offset from the LO frequency. The measured blocker 1-dB gain compression point ($B_{1dB,CP}$) was +13dBm at 40MHz offset. The measured S_{11} and blocker NF are shown in Fig. 20, both for filter 1 configuration. The S_{11} is better than -10dB for F_{lo}<800MHz, and only degrades to -9dB at F_{lo} =1GHz. The S_{11} worsens at higher LO frequencies due to input parasitic capacitance from RDACs, input pads, package, etc. [20]. The measured NF was 7dB at F_{lo}=500MHz and worsens by only 4.5dB when a 0dBm CW blocker was present at 30MHz offset. This is consistent with the simulated phase noise of the LO divider (-165dBc/Hz at 30MHz offset). The blocker NF is fairly constant with OOB blocker offset (since phase noise of the frequency divider is flat over frequencies). The linearity, S_{11} and noise measurements did not vary appreciably between filter configurations.

Table I compares this work with recent designs. This work maintains the high linearity of prior FA work [17], especially with respect to close-in blockers, while achieving sharper filtering and higher suppression than prior art. Good S_{11} is achieved while not degrading the NF. Nevertheless, recent advances in N-path filter [9] and mixer-first receiver techniques [15] have shown promising results in achieving high small-signal linearity at large offsets while matching the performance of this work at lower offsets and in large-signal linearity. Hence, avenues of combining such techniques with ideas from this work and noise cancellation may lead to further improvements in state-of-the-art receiver design. Increasing number of interleaving paths also has benefits in terms of higher filter sharpness [16] and lower antenna reradiation [20] that can be explored in future work.

V. Conclusion

This paper detailed a time-interleaved FA-based receiver front end. By using two time-interleaved sampled-and-held circuits, sharper filtering is achieved while simultaneously

TABLE I
COMPARISON TABLE

Metric	Darvishi [7] ISSCC '13	Xu [4] JSSC '16	Murphy [11] JSSC '12	Lien [15] JSSC '18	Hameed [17] ISSCC '16	This Work
Architecture	*N*-path	*N*-path + DT Filtering	Noise cancelling mixer-first	Mixer-first with positive cap feedback	FA with S_{11} constraint	Time-interleaved FA
Technology	65nm	40nm	40nm	45nm SOI	65nm	65nm
RF Frequency (GHz)	0.1-1.2	0.1-0.7	0.08-2.7	0.2-8	0.1-1	0.1-1
RF Input	Differential	Differential	Single-ended	Differential	Single-ended	Differential
BW* (MHz)	8	6.4-9.6	4	20	2.5-40	2.5-40
Stop-band Rejection (Transition BW)	59dB (12×BW)	>70dB (~8.5×BW)	NA	>25dB (~4.5×BW)	>35dB (2.5×BW) >50dB (6.5×BW)	>45dB (1.7×BW) >70dB (4×BW)
In-band IIP_3 (dBm)	-12	NA	-20	0	+5	+8
Out-of-band IIP_3 (dBm)	+26 (Δf=6.25×BW)	+24 (Δf=4.7×BW)	+13.5 (Δf=20×BW)	+39 (Δf=4×BW)	+17 (Δf=1.2×BW)	+21 (Δf=1.2×BW)
Out-of-band IIP_2 (dBm)	NA	NA	+55	+88 (Δf=4×BW)	+60 (Δf=1.2×BW)	+64 (Δf=1.2×BW)
$B_{1dB,CP}$ (dBm)	+7 (Δf=6.25×BW)	+14.7 (Δf=4.7×BW)	-2 (Δf=20×BW)	+8 (Δf=2×BW) +12 (Δf=4×BW)	+0.7 (Δf=2×BW) +8 (Δf=4×BW)	+9.5 (Δf=2×BW) +13 (Δf=4×BW)
S_{11} (dB)	-5 to -8	<-10	<-8.8	<-10	<-10	<-9
Gain (dB)	25	40	72	21	18.9	23
NF (dB)	2.8#	6.8-9.7#	1.9	2.3-5.4# (0.5-6GHz F_{lo})	6-7.5	6.5-8.5#
Supply Voltage (V)	1.2	1.2/1.6	1.2/2.5	1.2	1.2/1	1.2/1
Power Consumption	18-57.6mW	59-105mW	35.1-78mW	50mW+30mW/GHz	66.8-74mW	75-99+mW
Area (mm^2)	0.27	1.2	1.2	0.8	2	2.3

*RF bandwidth (twice the baseband bandwidth)

#Excludes balun loss

+Varies with F_{lo} (86mW for F_{lo}=0.5GHz)

maintaining a good S_{11}. Techniques were introduced for alleviating important circuit parasitics, while requirements on matching between time-interleaved paths were also derived. Measurement results indicate that the filter stop-band suppression achieved is higher than 70dB with a transition band of only 4 times the RF bandwidth.

REFERENCES

[1] Abidi, A.A., "The Path to the Software-Defined Radio Receiver," Solid-State Circuits, IEEE Journal of , vol.42, no.5, pp.954,966, May 2007.

[2] Nekovee, M., "Cognitive Radio Access to TV White Spaces: Spectrum Opportunities, Commercial Applications and Remaining Technology Challenges," New Frontiers in Dynamic Spectrum, 2010 IEEE Symposium on , vol., no., pp.1,10, 6-9 April 2010.

[3] Tohidian, M., et al., "3.8 A fully integrated highly reconfigurable discrete-time superheterodyne receiver," in Solid-State Circuits Conference Digest of Technical Papers (ISSCC), 2014 IEEE International , vol., no., pp.1-3, 9-13 Feb. 2014.

[4] Xu, Y., et al., " A Switched-Capacitor RF Front End With Embedded Programmable High-Order Filtering," IEEE J. Solid-State Circuits, vol.51, no.5, pp.1154-1167, May 2016.

[5] El Oualkadi, A., et al., "Fully Integrated High-Q Switched Capacitor Bandpass Filter with Center Frequency and Bandwidth Tuning," Radio Frequency Integrated Circuits (RFIC) Symposium, 2007 IEEE , vol., no., pp.681,684, 3-5 June 2007.

[6] Ghaffari, A., et al., "Tunable High-Q N-Path Band-Pass Filters: Modeling and Verification," Solid-State Circuits, IEEE Journal of , vol.46, no.5, pp.998,1010, May 2011.

[7] Darvishi, M., et al., "A 0.1-to-1.2GHz tunable 6th-order N-path channel-select filter with 0.6dB passband ripple and +7dBm blocker tolerance," in Solid-State Circuits Conference Digest of Technical Papers (ISSCC), 2013 IEEE International , vol., no., pp.172-173, 17-21 Feb. 2013.

[8] Hameed, S., et al., "Frequency-Domain Analysis of N-path Filters Using Conversion Matrices," Circuits and Systems II: Express Briefs, IEEE Transactions on , vol.63, no.1, pp.74-78, Jan. 2016.

[9] Lien, Y., et al., "A high-linearity CMOS receiver achieving +44dBm IIP3 and +13B1dB for SAW-less LTE radio", Solid-State Circuits Conference Digest of Technical Papers (ISSCC), 2017 IEEE International , vol., no., pp.412,413, 4-8 Feb. 2017.

[10] Andrews, C.; Molnar, A.C., "Implications of Passive Mixer Transparency for Impedance Matching and Noise Figure in Passive Mixer-First Receivers," Circuits and Systems I: Regular Papers, IEEE Transactions on , vol.57, no.12, pp.3092,3103, Dec. 2010.

[11] Mirzaei, A.; Darabi, H., "Analysis of Imperfections on Performance of 4-Phase Passive-Mixer-Based High-Q Bandpass Filters in SAW-Less Receivers," Circuits and Systems I: Regular Papers, IEEE Transactions on , vol.58, no.5, pp.879,892, May 2011.

[12] Murphy, D., et al., "A Blocker-Tolerant, Noise-Cancelling Receiver Suitable for Wideband Wireless Applications,"in Solid-State Circuits, IEEE Journal of , vol.47, no.12, pp.2943-2963, Dec. 2012.

[13] Run Chen; Hashemi, H., "19.3 Reconfigurable SDR receiver with enhanced front-end frequency selectivity suitable for intra-band and inter-band carrier aggregation," in Solid- State Circuits Conference - (ISSCC), 2015 IEEE International , vol., no., pp.1-3, 22-26 Feb. 2015.

[14] Hameed, S., et al., "Frequency-domain analysis of a mixer-first receiver using conversion matrices", Circuits and Systems (ISCAS), 2015 IEEE International Symposium on , vol., no., pp.541,544, 24-27 May 2015.

[15] Lien, Y.C., et al., "Enhanced-Selectivity High-Linearity Low-Noise Mixer-First Receiver With Complex Pole Pair Due to Capacitive Positive Feedback", Solid-State Circuits, IEEE Journal of , vol.53, no.5, pp.1348-1360, May 2018.

[16] M. Rachid, et al., "Filtering by Aliasing," in Signal Processing, IEEE Transactions on , vol.61, no.9, pp.2319-2327, May1, 2013.

[17] Hameed, S, et al., "A programmable receiver front-end achieving >17dBm IIP3 at <1.25×BW frequency offset", Solid-State Circuits Conference Digest of Technical Papers (ISSCC), 2016 IEEE International , vol., no., pp.446,447, 31 Jan.-4 Feb. 2016.

[18] Hameed, S.; Pamarti, S., "Design and Analysis of a Programmable Receiver Front End Based on Baseband Analog-FIR Filtering Using an LPTV Resistor", Solid-State Circuits, IEEE Journal of , vol.53, no.6, pp.1592-1606, June 2018.

[19] Hameed, S.; Pamarti, S., "A time-interleaved filtering-by-aliasing receiver front-end with >70dB suppression at <4×bandwidth frequency

offset", Solid-State Circuits Conference Digest of Technical Papers (ISSCC), 2017 IEEE International , vol., no., pp.418,419, 4-8 Feb. 2017.
[20] Hameed, S.; Pamarti, S., "Impedance Matching and Reradiation in LPTV Circuits: An Analysis Using Conversion Matrices", Circuits and Systems I: Regular Papers, IEEE Transactions on , vol.65, no.9, pp.2842,2855, Sept. 2018.

Sameed Hameed (S'13–M'17) received the B.Tech. degree from IIT Madras, India, in 2011, and the M.S. and the Ph.D. degrees from the University of California, Los Angeles (UCLA), CA, USA, in 2013 and 2017, respectively, all in electrical engineering.

In 2013, he joined Broadcom, Irvine, CA, USA as an RFIC Design Intern. From 2016 to 2017, he was an RFIC Design Intern at Silvus Technologies, Los Angeles, CA, USA, where he is currently an RFIC Engineer. His current research interests include RF transceiver designs with an emphasis on signal processing techniques.

Dr. Hameed was a recipient of an Electrical Engineering Department Fellowship in 2013 for placing first in the 2013 Ph.D. Preliminary examination in circuits and embedded systems, a UCLA Graduate Division Fellowship in 2014, the Broadcom UCLA Fellowship during the 2015-2016 academic year, the Dissertation Year Fellowship and the MediaTek UCLA Fellowship during the 2016-2017 academic year, the IEEE SSCS 2015-2016 Predoctoral Achievement Award, the 2016-2017 SSCS Student Travel Grant, and the UCLA Electrical Engineering Department's 2016-2017 Distinguished Ph.D. Dissertation in Circuits and Embedded Systems Award. He has served as a reviewer for the IEEE TRANSACTIONS ON CIRCUITS AND SYSTEMS I and II.

Sudhakar Pamarti (S'98–M'03) received the B.Tech. degree in electronics and electrical communication engineering from IIT Kharagpur, India, in 1995, and the M.S. and the Ph.D. degrees in electrical engineering from the University of California, San Diego, CA, USA, in 1999 and 2003, respectively.

From 1995 to 1997, he was at Hughes Software Systems, New Delhi, India, and from 2003 to 2005, he was at Rambus Inc., Sunnyvale, CA, USA, involved in developing embedded software and firmware for a wireless communication system, and high speed I/O circuits, respectively. He is currently a Professor of electrical and computer engineering with the University of California, Los Angeles, CA, USA. His current interests include integrated circuit designs with a special focus on developing algorithmic techniques to overcome circuit impairments.

Dr. Pamarti was a recipient of the National Science Foundation's CAREER Award. He has served as an Associate Editor for the IEEE TRANSACTIONS ON CIRCUITS AND SYSTEMS I and II. He currently serves on the Technical Program Committee of the IEEE Custom Integrated Circuits Conference and the IEEE International Solid-State Circuits Conference.